Monthly Notices of the ROYAL ASTRONOMICAL SOCIETY

MNRAS **511,** 3428–3439 (2022) https://doi.org/10.1093/mnras/stac098
Advance Access publication 2022 February 17

The progenitor of the Vela pulsar

C. S. Kochanek [1,2]★

[1]*Department of Astronomy, The Ohio State University, 140 West 18th Avenue, Columbus OH 43210, USA*
[2]*Center for Cosmology and AstroParticle Physics, The Ohio State University, 191 W. Woodruff Avenue, Columbus OH 43210, USA*

Accepted 2022 January 10. Received 2022 January 10; in original form 2021 October 21

ABSTRACT

With *Gaia* parallaxes, it is possible to study the stellar populations associated with individual Galactic supernova remnants (SNRs) to estimate the mass of the exploding star. Here, we analyse the luminous stars near the Vela pulsar and SNR to find that its progenitor was probably ($\gtrsim 90$ per cent) low mass (8.1–10.3 $M_\odot$). The presence of the O star γ^2 Vel a little over 100 pc from Vela is the primary ambiguity, as including it in the analysis volume significantly increases the probability (to 5 per cent) of higher mass ($> 20\,M_\odot$) progenitors. However, to be a high-mass star associated with γ^2 Vel's star cluster at birth, the progenitor would have to be a runaway star from an unbound binary with an unusually high velocity. The primary impediment to analysing large numbers of Galactic SNRs in this manner is the lack of accurate distances. This can likely be solved by searching for absorption lines from the SNR in stars as a function of distance, a method which yielded a distance to Vela in agreement with the direct pulsar parallax. If Vela was a $10\,M_\odot$ supernova in an external galaxy, the 50-pc search region used in extragalactic studies would contain only $\simeq 10$ per cent of the stars formed in a 50-pc region around the progenitor at birth and $\simeq 90$ per cent of the stars in the search region would have been born elsewhere.

Key words: stars: massive – supernovae: general.

1 INTRODUCTION

We would like to understand which massive stars explode as supernovae and the nature of the resulting compact objects. Modern theoretical models (e.g. O'Connor & Ott 2011; Pejcha & Thompson 2015; Ertl et al. 2016, Sukhbold et al. 2016; Ghosh, Wolfe & Fröhlich 2021) find a complex mapping between progenitor mass and explosion driven by changes in core structure related to the balance between radiative and convective carbon burning (Sukhbold, Woosley & Heger 2018; Sukhbold & Adams 2020). In these modern models, essentially all stars either explode and produce neutron stars or fail to explode and produce black holes – 'fall back' supernovae where the star explodes but a significant amount of mass falls back on to the proto-neutron star to form a black hole are extremely rare.[1] In the absence of fall back, lower mass ($\lesssim 10\,M_\odot$) black holes are produced either from explosions of stars stripped by pre-supernova mass-loss/transfer or by the failed explosions of the more massive red supergiants. These produce black holes with the mass of the helium core (Kochanek 2014) because the Nadezhin (1980) mechanism (also see e.g. Lovegrove & Woosley 2013; Fernández et al. 2018) ejects the weakly bound hydrogen envelope of the supergiant. None of these surveys of outcomes are based on full *ab initio* core collapse simulations but instead use 'calibrated' explosion models to explore outcomes. The outcomes in true core collapse simulations remain an open problem because of the complexity of the physics and the need for high resolution three-dimensional (3D) simulations (e.g. Burrows et al. 2020; Bollig et al. 2021; Pan et al. 2021)

To test these theoretical predictions, we need to observationally determine the mapping between progenitors and outcomes. The cleanest approach for the stars which explode is simply to measure the properties of the progenitor star, as first done for SN 1987A (Gilmozzi et al. 1987). Since the stellar luminosity is determined by the mass of the core, and the mass of the core is determined by the initial mass of the progenitor, this is a fairly robust approach if there is sufficient data to well-determine the luminosity (although the mass at the time of explosion cannot be well-constrained, see Farrell et al. 2020). The challenge is that this must be done in distant (∼1–10 Mpc) galaxies and largely depends on the existence of multi-band archival *Hubble Space Telescope* data for robust results. The progenitors of Type IIP supernovae are red supergiants with an upper mass limit that is consistent with the theoretical explosion studies (Smartt et al. 2009; Smartt 2009, 2015), although there are rebutted (e.g. Kochanek, Khan & Dai 2012; Beasor et al. 2020; Kochanek 2020) counterarguments (e.g. Walmswell & Eldridge 2012; Groh et al. 2013; Davies & Beasor 2020). Less is known about the progenitors of Type Ibc supernovae because they are generally undetected, which likely implies that in most cases the envelopes are stripped by binary processes (e.g. Eldridge et al. 2013; Folatelli et al. 2016; Johnson, Kochanek & Adams 2017; Kilpatrick et al. 2021). Unfortunately, the nature of the compact remnant formed in these systems will likely always be unknown.

Failed supernovae can be found by searching for stars which disappear independent of the nature of any associated transient (Kochanek et al. 2008). A search for failed supernovae using the Large Binocular Telescope (Gerke, Kochanek & Stanek 2015; Adams

★ E-mail: ckochanek@astronomy.ohio-state.edu

[1]Despite this, fall back models for remnant masses such as Fryer et al. (2012) remain in common use for binary population synthesis models (e.g. Eldridge et al. 2017; Belczynski et al. 2020; Breivik et al. 2020; Chawla et al. 2021; Riley et al. 2021).

et al. 2017b; Neustadt et al. 2021) has identified one excellent candidate (Gerke et al. 2015; Adams et al. 2017a; Basinger et al. 2020) and a second, weaker candidate (Neustadt et al. 2021). As expected, the progenitor of the strong candidate was a massive RSG, and finding one candidate implies a fraction of core collapses leading to failed supernovae consistent with the current theoretical predictions.

The primary alternative to searching for individual progenitors is to use the local stellar population to infer the probable mass of the progenitor. This has been done for supernova remnants (SNRs) in the Magellanic Clouds (Badenes et al. 2009; Auchettl et al. 2019) and in nearby galaxies (e.g. Jennings et al. 2012, 2014; Díaz-Rodríguez et al. 2018, 2021; Williams et al. 2018, 2019; Koplitz et al. 2021). Except for Williams et al. (2018) and Díaz-Rodríguez et al. (2021), which examine stellar populations near known supernovae, these are studies of the stellar populations near SNRs. The primary advantage of this method is that it can be applied to large numbers of SNRs or historical supernovae compared to the numbers of directly observed progenitors. For the Magellanic Clouds, several of the remnants are associated with neutron stars (N49, N158A and possibly SN 1987A in the LMC, and 1KT6 and 1E 0102.2−7219 in the SMC, see Badenes et al. 2009; Auchettl et al. 2019), so the outcome of the explosion is also known.

There are also several disadvantages. First, unless the local stellar population has a single well-defined starburst, the method does not provide individual well-constrained masses and so is best suited for making statistical models of the progenitor distribution. Secondly, the nature of the supernova is unknown for SNRs, so, for example, one cannot separately investigate the progenitors of Type IIP and Type Ibc supernovae. No SNR studies can directly address the deficit of more massive RSG progenitors to Type IIP supernovae because the supernova types are unknown. Thirdly, the lifetime and detectability of the SNR has some dependence on the nature of the explosion (e.g. Sarbadhicary et al. 2017; Jacovich et al. 2021) which will introduce some bias into the results. Most, but not all, of these studies have supported a deficit of higher mass SN progenitors. The progenitor mass distribution models used to date in these studies are simple functional forms that do not resemble current theoretical expectations, so it is difficult to evaluate the degree to which they agree or disagree with these expectations.

With the advent of *Gaia* (Gaia Collaboration et al. 2016; 2021), it is now possible to apply this second method to Galactic SNRs if the distance to the remnant is known and the extinction is not severe. The present number of such systems is small, primarily because so few SNRs have well-constrained distances. As with extragalactic SNRs, the supernova type will generally be unknown, but, unlike extragalactic SNRs, the compact object outcome of the explosion frequently is known. Because the Galaxy is so well-surveyed from the mid-IR into the ultraviolet, it will generally be possible to characterize the individual stars extremely well, with well-determined individual stellar luminosities, temperatures, and extinctions. In many cases, the brighter stars will also have spectroscopic classifications. Here, we demonstrate this for the Vela pulsar (PSR J0835−4510, PSR B0833−45, Large, Vaughan & Mills 1968), which is so nearby (280 pc, Dodson et al. 2003) that many of the massive stars near it are visible to the naked eye. We describe the selection of the stars and spectral energy distribution (SED) models of the more luminous stars in Section 2. We analyse these stars to estimate the likely mass of Vela's progenitor in Section 3; and we discuss the results and future prospects in Section 4.

2 SELECTING THE STARS

We select the stars from the Gaia EDR3 catalogue (Gaia Collaboration et al. 2016, 2021), requiring them to have parallaxes, proper motions, and all three *Gaia* magnitudes. We apply no restriction on the RUWE statistic for the quality of the parallax. We adopt the position (J2000 08:35:20.61149 ± 0.00002, −45:10:34.8751 ± 0.0003), parallax ($\varpi = 3.5 \pm 0.2$ mas), and proper motions ($\mu_\alpha = -49.68 \pm 0.06$ and $\mu_\delta = 29.9 \pm 0.1$ mas yr^{-1}) of the pulsar from Dodson et al. (2003). The parallax is sufficiently accurate that it is essentially unaffected by Lutz–Kelker bias (see Verbiest et al. 2012). The spin-down age of Vela is 11.3 kyr, although Lyne et al. (1996) argue that the braking index implies a larger age. The proper motions combined with the offset from the centre of the remnant imply an age of 18000 ± 9000 years based on the 25 ± 5 arcmin offset of the pulsar from the centre of the remnant (Aschenbach, Egger & Trümper 1995). Unfortunately, Aschenbach et al. (1995) do not report their estimated position for the centre, but if we adopt an age of $T =$ 20000 years we can estimate the position of the explosion from the position shift of (+17, −10) arcmin. The remnant itself has a diameter of approximately 8.3 degrees, so the shift is small compared to the scale of the remnant and the size of our search region. We select the stars in a region centered on the shifted equatorial position of (128.°84, −45.°18) where we have reduced the coordinate precision due to the uncertain age.

The next question is the size of the region to extract around Vela to obtain a representative stellar population. The studies of the regions around supernovae and SNRs in nearby galaxies have almost uniformly used a region 50 pc in radius based on the argument that stars form in compact clusters (∼1 pc, Lada & Lada 2003), drift apart at low relative velocities (∼km s^{-1}), and that stars which explode after their parent binary was disrupted by a supernova have only modest velocities (Eldridge, Langer & Tout 2011; Renzo et al. 2019). With *Gaia*, we can simply consider this question empirically. In this section, we consider the 3D geometry we use for Vela; and in Section 4, we consider the 2D projected geometry of extragalactic analyses.

We started by extracting all stars within $R = 250$ pc of Vela. If the pulsar is at a distance of $D = 286$ pc, a sphere of radius R subtends a maximum angle of $\theta = \sin^{-1} R/D \simeq 62$ deg relative to its centre. We select stars with $\theta < 62$ deg, $1.87 < \varpi < 28.6$ mas, which corresponds to ±250 pc around the pulsar distance, and $G < 9.5$ mag. This will include all stars with $M_G \lesssim 0$ mag since the extinctions are small. At this magnitude limit, we are including all $M \gtrsim 5\,\mathrm{M}_\odot$ stars and the more luminous, evolved, lower mass stars. The initial search yields ∼55 000 stars, of which ∼37 000 are within $R = 250$ pc of the pulsar, and 3160 are brighter than $M_G < 0$ mag.

The bright magnitude limit of *Gaia* at $G \simeq 3$ mag can be a problem because the most luminous stars may not be present in the *Gaia* catalogue. We searched the *Hipparcos* (Perryman et al. 1997, using the updated astrometric solution from van Leeuwen 2007) and the Bright Star (Hoffleit & Warren 1995) catalogues for any such stars in the search volume, finding nine *Hipparcos* stars: HIP 30324 (β CMa) HIP 33579 (ϵ CMa), HIP 39953 (γ^2 Vel), HIP 41037 (ϵ Car) HIP 44816 (λ Vel), HIP 66657 (ϵ Cen) HIP 68702 (ζ Cen), and HIP 81173 (α TrA). Since γ^2 Vel is in a wide binary (Tokovinin 2018) with γ^1 Vel (HD 68243), we use the *Gaia* parallax of γ^1 Vel for γ^2 Vel. For the other stars, we adopt the updated *Hipparcos* parallaxes. Including the bright *Hipparcos* stars, there are $N = 3169$ stars with $M_G < 0$ mag within $R = 250$ pc of Vela. Fig. 1 shows the distribution of the $R < 125$ pc stars in absolute magnitude M_G and colour $B_P - R_P$ (with no extinction corrections) as compared to

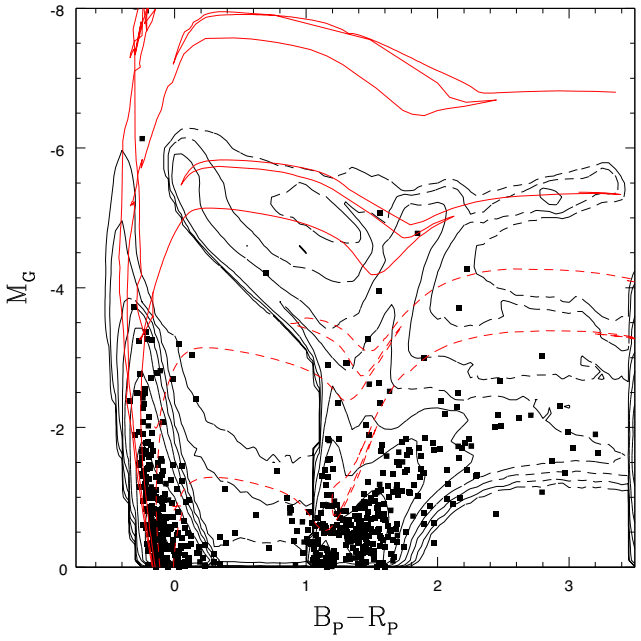

Figure 1. Colour-magnitude diagram without extinction corrections for the stars with $M_G > 0$ mag and within $R < 125$ pc of Vela. The background contours are the maximum likelihood model for the stellar density including extinction with solid (dashed) contours at higher (lower) densities that are spaced by factors of 3. The red curves are Solar metallicity PARSEC isochrones with ages of $10^{8.5}$ (bottom, dashed), $10^{8.0}$ (dashed) $10^{7.5}$ (solid), $10^{7.0}$ (solid), and $10^{6.6}$ (top, solid) years. The maximum mass for the $10^{7.5}$ yr isochrone is 9.1 $M_\odot$, so only the solid isochrones still have stars which will explode as supernovae. The isochrones are shifted by the mean extinction of $E(B-V) = 0.057$ mag. The photometric uncertainties are generally significantly less than 0.01 mag for these bright stars.

Solar metallicity PARSEC (Bressan et al. 2012; Marigo et al. 2013; Pastorelli et al. 2020) isochrones with ages of $10^{6.6}$, $10^{7.0}$, $10^{7.5}$, $10^{8.0}$, and $10^{8.5}$ yr. For the bright *Hipparcos* stars, we used the SED fits described below to synthesize the *Gaia* magnitudes.

2.1 Completeness and contamination

To explore optimizing the region from which we select stars, we only want to consider the younger, massive stars. The main contaminants are lower mass red giants, which we can largely remove by considering only stars with $M_G < 0$ for $B_P - R_P < 0.6$, $M_G < -2.0$ for $0.6 < B_P - R_P < 1.8$, and $M_G < -3.5$ for $B_P - R_P > 1.8$. Only a small fraction of the stars have Gaia DR2 radial velocities, so we assigned a random line-of-sight velocity with a dispersion of 3.0 km s^{-1} based on the velocity dispersion derived from the proper motions of the stars within 50 pc of Vela (see below).

In our present analysis, we are selecting the stars in 3D, so we want to explore the effect of changing the radius of the selection sphere. We can estimate the completeness and contamination of the selection by examining the relative positions of the stars today and in the past. We start by taking the stars near the pulsar and determining where they were 10^7 and $10^{7.5}$ yr in the past – these roughly correspond to the lifetimes of 20 and 10 $M_\odot$ stars, respectively. Because the pulsar received a kick, we cannot do the same for the past location of the progenitor star. For simplicity, we assume that the progenitor had the mean velocity of the stars. The completeness will be lower if we include a random motion for the progenitor.

Following the extragalactic studies, we first considered a 50-pc sphere. This sphere around Vela today contains 19 of these young, high-mass stars. After subtracting their median tangential velocities, they have a 2D velocity dispersion of 4.2 km s^{-1} defined by half the width of the velocity range encompassing 68 per cent of the stars. As we expand the radius of the sphere, the number of stars rises rapidly to 152, 411, 757, and 1160 within 100, 150, 200, and 250 pc, and the 2D velocity dispersion rises slowly to 5.4, 6.7, 6.7, and 7.9 km s^{-1}, respectively. We used the 4.2 km s^{-1} dispersion derived from the proper motions to set the $4.2/\sqrt{2} = 3.0$ km s^{-1} dispersion of the randomly assigned line-of-sight velocity. The 3D velocity dispersion is then 5.1 km s^{-1}, so the typical typical massive star has a random motion of $\simeq$50 pc in the lifetime of a $\sim 20\,M_\odot$ star ($\sim 10^7$ yr) and $\simeq$ 150 pc in the lifetime of a $\sim 10\,M_\odot$ star ($\sim 10^{7.5}$ yr).

If we place a sphere at the median position of these stars 10^7 yr ago, we can estimate the completeness and contamination. The completeness is the fraction of stars inside a sphere of some radius today that are inside a sphere of some other radius centered at the median position of the stars in the past. The contamination is the fraction of the stars in the 'past sphere' that were not in the 'present sphere'. For a 50-pc sphere today, 4, 12, 16, and 18 of the 19 stars are in a past sphere of radius 50, 100, 150, and 200 pc, along with 10, 61, 179, and 356 stars which were not in the 50-pc sphere today. So the completeness are 21, 63, 84, and 95 per cent, while the contamination rates are 71, 84, 92, and 95 per cent. Basically, since the typical random motion corresponds to moving 50 pc in 10^7 yr, a sphere of comparable size must suffer from poor completeness and significant contamination. Table 1 summarizes these results and those of present spheres of radius 100 and 150 pc for a past sphere 10^7 and $10^{7.5}$ yr ago. Needless to say, the completeness and contamination are significantly worse if we use the $10^{7.5}$ yr lifetime of a $\simeq 10\,M_\odot$ star.

Completeness and contamination are, of course, a trade off – there is no right answer. We will present all of our results for a radius of 125 pc. We were originally going to use 100 pc but the most massive star near Vela, γ^2 Vel, lies just outside a 100 pc sphere, so we increased the radius to 125 pc to double the volume and include γ^2 Vel. For the final results on the probable age and mass of Vela's progenitor, we will present the results for a range of radii.

2.2 SED models of the more luminous stars

We fit the SEDs of the more luminous stars in the 125-pc sphere to estimate their luminosity, temperature, and extinctions. We also fit the bright *Hipparcos* stars to synthesize their *Gaia* magnitudes. The SED fits are moderately labour intensive in terms of collating the data, so we did not model all the lower luminosity stars. We initially selected all stars with $M_G < -2$ ($M_G < -3.5$) for $B_P - R_P < 1.8$ (>1.8), where the higher luminosity limit for redder stars eliminates lower mass red giants. While the SEDs showed no need to include circumstellar dust, we used the same methods as in Adams et al. (2017a), running DUSTY (Elitzur & Ivezić Ž. 2001) inside a Markov chain Monte Carlo (MCMC) driver to both optimize the fits and then estimate the uncertainties. We used Castelli & Kurucz (2003) model atmospheres for all but the coolest stars where we used MARCS (Gustafsson et al. 2008) model atmospheres. We used near-IR data from 2MASS (Cutri et al. 2003). The optical data primarily came from Johnson et al. (1966) and Tonry et al. (2018), supplemented by Cousins (1971), Ducati (2002), Mermillod (1977), Morel & Magnenat (1978), NOMAD (Zacharias et al. 2005), and Neckel & Klare (1980). Almost all of the hot stars had UV data extending to ~1500 Å from either Thompson et al. (1978) or Wesselius et al. (1982).

Table 1. Completeness and contamination.

Present sphere	Past sphere – $10^{7.0}$ yr ago			
(pc)	50 pc	100 pc	150 pc	200 pc
50	21 /71	63/84	84/92	95/95
100		36/21	68/47	84/67
150			40/14	70/25
		Past Sphere - $10^{7.5}$ yr ago		
50	5/75	16/79	26 /88	47/89
100		3 /61	9 /61	22/58
150			7/15	15/25
		Past Cylinder - $10^{7.0}$ yr ago		
50	79/47	84/90		
100		58/50	76/63	
		Past Cylinder - $10^{7.5}$ yr ago		
50	11/89	26/90		
100		14/56	28/64	

Note. Completeness/contamination where the completeness is the fraction of stars within the 'Present Sphere' that are in the 'Past Sphere' $10^{7.0}$ or $10^{7.5}$ yr ago. The contamination is the fraction of stars in the 'Past Sphere' which were not in the 'Present Sphere'. All entries are percentages.

We used temperature priors based on the reported spectral types in SIMBAD (Wenger et al. 2000) and weak extinction priors. The temperature prior widths were roughly one spectral type (so B1–B3 for a B2 star) and ±0.1 mag for $E(B-V)$. For extinction priors, we use the 3D `combined19 mwdust` models (Bovy et al. 2016), which combine the Drimmel, Cabrera-Lavers & López-Corredoira (2003), Marshall et al. (2006), and Green et al. (2019) models to provide estimates for any sky position. We extracted the V-band extinction, and then used an $R_V = 3.1$ extinction law to convert the V-band extinction to those for the G, B_P, and R_P bands. For most stars, the SEDs could only modestly improve the spectral temperature estimates but strongly constrained the extinction. The agreement with the `mwdust` estimates was generally good, except when the `mwdust` estimate was high ($E(B-V) \gtrsim 0.1$). In these cases, the SED models generally required much less dust. With this caveat, we will use the `mwdust` extinctions to model the effects of extinction for the full sample.

Table 2 gives the goodness of fits, temperature, luminosity, mass, age, separation from estimated explosion centre, and some comments for the stars with $L_* > 10^{3.5}\,L_\odot$. This luminosity limit is simply chosen as a round number that will include all stars expected to explode. The individual masses and ages are simply the range of PARSEC isochrone ages and masses where the luminosity and temperature are within twice the estimated uncertainties of the fitted values with a minimum uncertainty of 0.02 dex. The ages and masses are strongly correlated – the maximum masses correspond to the minimum ages and *vice versa*. Except for γ^2 Vel, they are all less massive than $\simeq 15\,M_\odot$ and older than $\simeq 10^7$ years even for the upper (lower) limits on the masses (ages).

2.3 Binaries

While many of the stars are binaries (see Table 2), the extra light from the secondary seems to have little consequence for the SED fits. This is not very surprising because B stars are still in the regime where the mass–luminosity relation is fairly steep and a modestly lower mass companion will not greatly perturb the SED. For example, consider the most luminous star, γ^2 Vel, which is an O star plus Wolf–Rayet (WR) star binary. γ^2 Vel is an interferometrically resolved double lined spectroscopic binary with present day masses of (28.5 ± 1.1) and $(9.0 \pm 0.6)\,M_\odot$ for the O star and the companion WR star, respectively (North et al. 2007). While our SED fit finds a higher total luminosity, most of the difference is due to both the Gaia EDR3 distance (where we used the distance to the wide binary companion γ^1 Vel) and our extinction estimate being larger than those used by North et al. (2007). Still, our rough individual mass estimate of 25.3–27.3 $M_\odot$ agrees reasonably well with their dynamical measurement. North et al. (2007) estimate that only 22 per cent of the V-band light comes from the WR star, so the SED fit itself is not strongly biased by the WR companion.

More quantitatively, if $L \propto M^x$ with $x \simeq 3$, then the luminosity of a binary with mass ratio $q < 1$ is $1 + q^3$ larger than that of the primary. The mass estimate for the primary, ignoring the secondary, is then $(1 + q^3)^{1/3}$. Even the mass of a twin $q = 1$ binary is only overestimated by 25 per cent and the known binaries seem to generally have significant mass ratios. For a mass ratio $q = 0.7$, the mass bias has already dropped to 10 per cent.

3 THE PROGENITOR OF VELA

The striking property of Figs 1 and the models in Table 2 is the marked absence of very young stars or massive stars with the exception of γ^2 Vel. All of the other stars are only consistent with populations older than 10 million yr, corresponding to maximum progenitor masses $\lesssim 15\,M_\odot$. The next step is to use these stars to estimate the mass of the progenitor of the Vela pulsar. Here, we will model the *Gaia* colour–magnitude distribution to estimate the numbers of stars as a function of age. As discussed in Section 2, we present all of the results for a 125-pc sphere around Vela, and the estimated age/mass of the progenitor for regions from 100 to 200 pc in radius. We include all stars with $M_G < 0$ before extinction corrections (i.e. the magnitude range shown in Fig. 1).

3.1 Method

We will assume a Salpeter (1955) initial mass function (IMF) with a minimum mass of $M_{\rm min} = 1\,M_\odot$ since we are not interested in the lower mass stars. If the star formation rate ($M_\odot\,{\rm yr}^{-1}$) for $M > M_{\rm min}$ stars is SFR, then the rate of forming stars is

$$\frac{{\rm d}N}{{\rm d}t\,{\rm d}M} = \frac{(x-2)SFR}{M_{\rm min}^2}\left(\frac{M}{M_{\rm min}}\right)^{-x}, \quad (1)$$

Table 2. Luminous stars near the Vela pulsar.

Star	$\chi^2/N_{\rm dof}$	$\log(T_*)$ (K)	$\log(L_*)$ ($L_\odot$)	M_* ($M_\odot$)	$\log t$ (yr)	Sep (pc)	Comments
HD 68273	0.79	4.622 ± 0.020	6.029 ± 0.070	25.3–27.3	6.61–6.63	102	γ^2 Vel, O7.5III + WC8 binary
HD 63462	1.82	4.383 ± 0.032	4.347 ± 0.094	9.8–13.9	6.96–7.40	124	O Pup, B1IVe
HD 68243	1.00	4.358 ± 0.033	4.319 ± 0.084	9.5–13.2	7.07–7.43	102	γ^1 Vel, B2III
HD 65818	1.74	4.390 ± 0.029	4.297 ± 0.075	9.9–13.4	6.92–7.39	92	V Pup, B1Vp + B2 ecl. binary
HD 74575	0.27	4.345 ± 0.018	4.149 ± 0.053	8.9–11.3	7.19–7.49	70	α Pyx, B1.5III
HR 3307	2.29	3.624 ± 0.012	4.137 ± 0.029	7.9–13.1	7.19–7.62	116	ϵ Car, K3III + B2 binary
HD 57150	1.03	4.325 ± 0.040	4.076 ± 0.121	7.7–11.5	7.10–7.61	83	υ^1 Pup, B2V + B3IV binary
HD 78647	2.03	3.618 ± 0.010	4.050 ± 0.044	2.0–12.1	7.25–8.73	121	λ Vel, K4I
HD 63032	1.53	3.619 ± 0.010	4.008 ± 0.036	2.0–11.7	7.27–8.74	84	c Pup, K4III
HD 65551	1.61	4.407 ± 0.014	3.988 ± 0.034	9.8–11.9	<7.27	51	N Pup, B2II/IV
HD 83058	0.57	4.345 ± 0.035	3.940 ± 0.098	7.6–10.8	6.84–7.62	90	L Vel, B2IV
HD 56139	2.75	4.246 ± 0.028	3.931 ± 0.087	7.3–9.3	7.42–7.66	120	ω CMa, B2.5Ve
HD 51799	2.58	3.597 ± 0.008	3.862 ± 0.034	1.9–10.0	7.38–8.75	122	M1III
HD 63465	0.93	4.261 ± 0.032	3.843 ± 0.108	6.6–9.3	7.41–7.75	105	B2IV/V
HD 68324	0.31	4.353 ± 0.028	3.835 ± 0.075	8.2–10.3	6.62–7.47	65	IS Vel, B2V
HD 64740	0.84	4.369 ± 0.024	3.800 ± 0.059	8.4–10.4	<7.42	56	B2V
HD 73155	1.78	3.671 ± 0.011	3.799 ± 0.040	6.6–9.5	7.43–7.78	90	C Vel, K1.5I
HD 68217	0.34	4.324 ± 0.034	3.772 ± 0.094	6.9–9.7	6.79–7.70	48	B2IV
HD 64503	0.44	4.307 ± 0.029	3.727 ± 0.081	6.8–9.0	7.17–7.72	64	b Pup, B2V binary
HD 65575	0.73	4.232 ± 0.029	3.661 ± 0.099	6.0–8.1	7.53–7.84	117	χ Car, B3IV
HD 57219	0.25	4.263 ± 0.030	3.643 ± 0.087	6.1–8.2	7.42–7.83	102	υ^2 Pup, B3Ve
HD 89388	1.63	3.639 ± 0.008	3.642 ± 0.035	5.2–8.7	7.50–8.03	112	q Car, K2.5II
HD 85123	0.75	3.879 ± 0.018	3.635 ± 0.041	6.0–7.4	7.64–7.86	108	υ Car, A9
HD 54893	0.32	4.282 ± 0.028	3.602 ± 0.082	6.2–8.2	7.30–7.80	83	A Pup, B3IV/V
HD 63949	0.58	4.286 ± 0.029	3.563 ± 0.091	6.2–8.1	7.21–7.81	112	QS Pup, B2III β Ceph
HD 79275	0.91	4.320 ± 0.025	3.509 ± 0.073	6.8–8.5	<7.60	63	B2III/IV
HD 56779	0.61	4.247 ± 0.024	3.490 ± 0.074	5.7–7.3	7.53–7.89	85	B3V
HD 69144	0.79	4.195 ± 0.025	3.487 ± 0.084	5.4–7.1	7.66–7.94	82	NO Vel, B3III ecl. binary
HD 84816	1.06	4.268 ± 0.026	3.465 ± 0.082	5.9–7.5	7.36–7.86	82	B2V
HD 85622	2.08	3.697 ± 0.012	3.438 ± 0.046	5.3–7.2	7.67–8.01	66	m Vel, G6IIa binary
HD 63922	0.42	4.152 ± 0.020	3.429 ± 0.053	5.6–6.4	7.77–7.92	40	P Pup, B7/8
HD 61641	0.78	4.246 ± 0.023	3.402 ± 0.073	5.6–7.0	7.51–7.92	106	e Pup, B3III
HD 59550	0.89	4.269 ± 0.020	3.401 ± 0.060	6.2–7.2	7.36–7.74	118	B2IV
HD 71510	0.41	4.298 ± 0.047	3.394 ± 0.132	5.6–8.6	<7.91	62	B3IV, Be star
HD 68895	0.70	4.203 ± 0.026	3.295 ± 0.086	5.0–6.5	7.67–8.04	104	B5V binary
HD 76566	1.02	4.244 ± 0.025	3.251 ± 0.080	5.5–6.6	7.36–7.84	89	B3IV
HD 75710	1.67	3.959 ± 0.005	3.251 ± 0.025	5.0–5.6	7.91–8.03	101	g Vel, A2III
HD 82150	4.19	3.630 ± 0.008	3.173 ± 0.042	2.5–6.2	7.81–8.93	92	ϵ Ant, K3III
HD 91504	0.28	3.675 ± 0.011	3.156 ± 0.029	4.5–6.2	7.81–8.18	121	t Vel, K1/2III
HD 72227	0.77	3.655 ± 0.012	3.129 ± 0.038	3.4–6.1	7.83–8.53	85	K3III
HD 92449	0.49	3.697 ± 0.013	3.105 ± 0.049	4.5–5.9	7.86–8.18	110	x Vel, G5II
HD 50235	0.16	3.646 ± 0.010	3.087 ± 0.029	2.5–5.9	7.86–8.91	111	K2/3III
HD 85355	0.95	4.100 ± 0.013	3.057 ± 0.040	4.5–5.1	7.99–8.14	66	n Vel, B7III
HD 75630	1.42	3.958 ± 0.006	3.027 ± 0.029	4.4–4.8	8.06–8.17	94	h Vel, A2/EIV
HD 49689	0.48	3.659 ± 0.015	3.026 ± 0.051	3.2–5.7	7.88–8.59	94	K3III
HD 65699	0.22	3.694 ± 0.013	2.933 ± 0.043	4.2–5.3	7.96–8.27	112	12 Pup, G9IIa pec
HD 68512	0.50	3.668 ± 0.013	2.922 ± 0.044	3.2–5.3	7.96–8.60	80	K3III
HD 85656	0.55	3.678 ± 0.012	2.863 ± 0.029	3.4–5.1	8.00–8.53	101	K1III
HD 76304	0.90	3.692 ± 0.009	2.708 ± 0.017	3.4–4.7	8.10–8.53	119	K0II/III
HD 80126	0.23	3.726 ± 0.012	2.696 ± 0.040	3.8–4.5	8.13–8.37	118	G8II

with $x = 2.35$ and a mean mass of $\langle M \rangle = (x-1)M_{\rm min}/(x-2)$. We divide the star formation history into logarithmic time intervals $t_{{\rm min},\,i} < t < t_{{\rm max},\,i}$ with $\Delta t_i = t_{{\rm max},\,i} - t_{{\rm min},\,i}$. Assuming the star formation rate SFR_i in the interval is constant, the number of $M > M_{\rm min}$ stars formed is

$$N_i = \frac{SFR_i \Delta t_i}{\langle M \rangle}. \tag{2}$$

The number of stars formed in this period which die in a short time interval δt today is

$$N_i \frac{\delta t}{\Delta t_i}\left[\left(\frac{M(t_{{\rm min},i})}{M_{\rm min}}\right)^{1-x} - \left(\frac{M(t_{{\rm max},i})}{M_{\rm min}}\right)^{1-x}\right] = N_i S_i \delta t, \tag{3}$$

where $M(t)$ is the most massive surviving star on the isochrone, and $S_i\delta t$ is the fraction of $M > M_{\rm min}$ stars that died in the last δt years. This expression is explicitly assuming single star evolution. We used eight temporal bins spanning $6.4 < \log t < 8.0$, bin widths of 0.2 dex and use the number N_i of $M > M_{\rm min}$ stars formed as the variable to be determined.

If the global IMF is Salpeter (1955) down to $0.5\,M_\odot$ and then flattens to $M^{-1.3}$ from 0.08 to $0.5\,M_\odot$ (Kroupa 2001), then the $M > M_{\rm min} = M_\odot$ stars represent 9.1 per cent of the stars formed. The global mean mass is $0.61\,M_\odot$, so for each $M > M_{\rm min} = M_\odot$ star formed, the total mass of new stars is $6.7\,M_\odot$. Local estimates of the mean stellar mass density are $0.04\,M_\odot\,{\rm pc}^{-3}$ (e.g. Flynn et al. 2006), so we should find $\sum N_i \simeq 6 \times 10^4$. If we use $2\pi R_d^2 H$ with $R_d = 3$ kpc and $H = 0.1$ kpc as the volume of the Galaxy, forming ten

$M > M_{\rm min} = {\rm M}_\odot$ stars per megayear in a 125-pc sphere (the scale of our formation rate estimate in Section 3.2) corresponds to a global star formation rate of $\sim 0.04\,{\rm M}_\odot\,{\rm yr}^{-1}$.

We start by building density maps ρ_i^{jk} in absolute magnitude M_G (index j) and colour $B_P - R_P$ (index k) for each time interval i. We use Solar metallicity PARSEC isochrones sampled at $\Delta \log t = 0.01$ dex. For each density map i, we carry out $N_{\rm trial}$ trials. We uniformly select a time between $t_{{\rm min},\,i}$ and $t_{{\rm max},\,i}$, which corresponds to assuming a constant star formation rate for each bin, randomly draw an initial stellar mass from the IMF, and use the isochrones to determine the absolute magnitude and colour if a star of this mass still exists.

For the magnitude range we consider, the uncertainties in the *Gaia* magnitudes are negligible (<0.01 mag). Similarly, the median parallax uncertainty of 0.027 mas is also unimportant given that the smallest parallax we consider is 2.43 mas. The median mwdust extinctions increase as $E(B-V) = 0.19(d\,{\rm kpc}^{-1})$ with distance d from the Sun. The width of the distribution is approximately $0.13(d\,{\rm kpc}^{-1})$. Since the mwdust estimates agreed reasonably well with the extinction estimates from the SED fits, we randomly assigned each trial the mwdust extinction of one of the $M_G < 0$ mag stars.

If the extincted trial star has $M_G < 0.0$ mag, we add $N_{\rm trial}^{-1}$ to the appropriate cell of ρ_i^{jk}. The maps span a finite range of colour ($-0.75 < B_P - R_P < 3.5$) and absolute magnitude ($0.0 > M_G > -8.0$) so trial stars that fall outside the colour range or are brighter than -8.0 mag are placed at the bin edge. This preserves the total probability for $M_G < 0.0$ mag stars. As we build the maps, we also build a binned mass distribution of the $M_G < 0.0$ mag stars, D_i^j for mass bin j. For $M_G < 0.0$ mag, we are including almost all $M > 5\,{\rm M}_\odot$ stars, and then only mass-dependent portions of the post-main sequence lifetimes of the lower mass stars.

With these definitions, the number distribution of stars in magnitude and colour brighter than the selection limit from time period i is $N_i \rho_{jk}^i$ and $N_i \sum_{jk} \rho_i^{jk} = N_i F_i$ is the number of stars still living and passing the selection criterion. F_i is the fraction of $M > M_{\rm min}$ stars which are more luminous than $M_g > 0$ mag. The expected number of stars in a colour/absolute magnitude bin is

$$e_{jk} = \sum_i N_i \rho_i^{jk}. \tag{4}$$

If we now distribute the N actual stars over the grid, the observed number of stars in a cell is n_{jk} with a Poisson probability of finding that number of stars of $e_{jk}^{n_{jk}} \exp(-e_{jk})/n_{jk}!$. The logarithm of the likelihood for all N stars is

$$\ln L = \sum_{\rm stars} \ln\left(\frac{r e_{ij}^{n_{ij}}}{n_{ij}!}\right) - \sum_{\rm all} r e_{ij}, \tag{5}$$

where the first term is the sum over bins containing stars and the second is the sum over all bins. Note that the factorial $n_{ij}!$ can be discarded since the calculation depends only on likelihood ratios and not the absolute likelihood. Putting trial stars falling off the grid when constructing the distributions on the bin edges ensures that the second sum is correct.

In equation (5), we have also introduced a 'renormalization' factor r. Equation (5) with $r = 1$ still includes the Poisson uncertainties from the total number N of stars being modelled. For the problem of estimating the progenitor mass, however, we need the relative probabilities (i.e. ratios) of the numbers of stars in the age bins, not their absolute values, and the ratios are unaffected by Poisson fluctuations from the finite number of stars. We solve this problem by optimizing the likelihood with respect to the renormalization factor to find that

$$r = N\left[\sum_{\rm all} e_{jk}\right]^{-1}, \tag{6}$$

which we then use to renormalize $N_i \rightarrow rN_i$. With this renormalization, $\sum_{all} e_{jk} \equiv N$ and we have effectively converted the Poisson likelihood into a multinomial likelihood for how to divide the N stars over the age bins.

Operationally, we optimize the likelihood and estimate the uncertainties using MCMC methods with the $\log N_i$ as the variables. Once trial values of $\log N_i$ are selected, they are renormalized before computing the likelihood. Some age bins were susceptible to $\log N_i \rightarrow -\infty$ (i.e. N_i arbitrarily close to zero), so we added a weak prior that the star formation rates of adjacent temporal bins should be similar by adding

$$\lambda^{-2} \sum_i \left[\ln\left(\frac{N_i\,\Delta t_{i+1}}{N_{i+1}\,\Delta t_i}\right)\right]^2, \tag{7}$$

with $\lambda = 6.91$ to the likelihood. This adds a penalty of unity to the likelihood if adjacent bins have star formation rates ($SFR_i \propto N_i/\Delta t_i$) that differ by a factor of 1000. This is just to prevent numerical divergences and has no significant effect on the results.

3.2 Properties of the local stellar population

Fig. 1 shows contours for the numbers of stars as a function of luminosity and temperature for the maximum likelihood model. Not surprisingly the maximum density lies along the main sequence of B stars. The density contours follow the stellar distribution closely. There are a few red giants in the very low probability density lower, right-hand corner. This may mean that there are some stars with higher extinctions than our model, probably cases which required some circumstellar dust. They are, however, old lower mass stars and should have no effect on the inferences about young, high mass stars.

Figs 2, 3, and 4 show three different ways of viewing the distribution of stars in age. Note that the error bars in these figures are highly correlated and the values cannot be independently adjusted by the scale of the error bars – the various analyses include the correlations since they use the full MCMC chains. Fig. 2 shows the distribution of the modelled stars, $N_i F_i$, in age. Because of the renormalization procedure, the numbers add up exactly to the $N = 607$ stars used. The five youngest age bins, corresponding to progenitors more massive than $10.3\,{\rm M}_\odot$ contain a median of $N_i F_i = 5$ modelled stars and fewer than 19 at 95 per cent confidence. For these young bins, we are basically counting all $M \gtrsim 5\,{\rm M}_\odot$ stars, so the number of higher mass stars is lower. For ten $M > 5\,{\rm M}_\odot$ stars and a Salpeter (1955) IMF, there are 3.9, 2.3, 1.5, and 0.9 stars more massive than 10, 15, 20, and $30\,{\rm M}_\odot$, respectively. The field contains very few high-mass stars, consistent with Fig. 1. For comparison, the $10^{7.4}$–$10^{7.6}$ yr bin, which spans a final mass range of 8.1–$10.3\,{\rm M}_\odot$ that corresponds to the minimum mass range expected to produce supernovae for single stars, has a median of $N_i F_i = 95$ modelled stars.

Only a small fraction of the $M > M_{\rm min}$ stars are luminous enough to be selected with $M_G > 0$ mag, so the actual number of stars associated with the older bins is much larger. Fig. 3 show the number N_i of $M > M_{\rm min}$ stars as a function of age. As expected, the total number of $M > M_{\rm min} = {\rm M}_\odot$ stars ($(6.8 \pm 2.3) \times 10^4$) in the volume is much larger than the 607 we modelled. And the total number of $M > 0.08\,{\rm M}_\odot$ stars would be another ~11 times larger. The implied

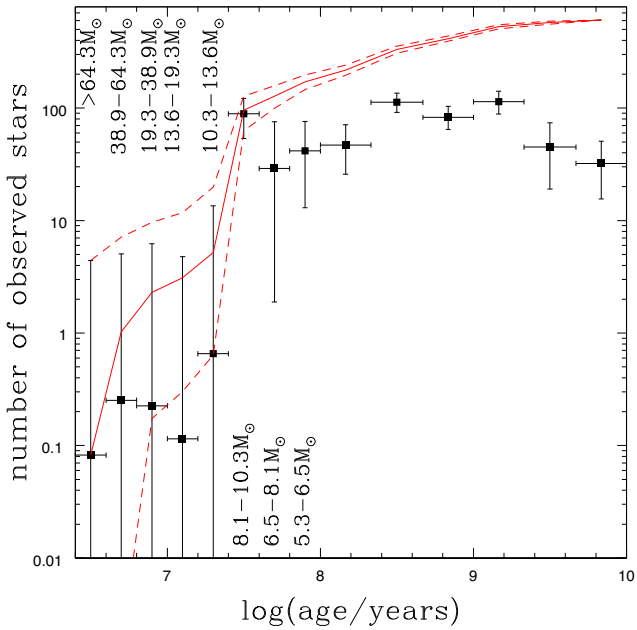

Figure 2. Age distribution N_iF_i of the modelled stars. The points show the median number of stars associated with each age bin and the 90-per cent confidence range. The horizontal error bars span the bin widths and the mass range corresponding to the more massive age bins is listed. The solid red curves shows the median integral distribution and the dashed curves show its 90-per cent confidence range. All uncertainties are highly correlated. The integral distribution converges exactly to the number of stars because we are determining how to distribute the modelled stars over the age bins.

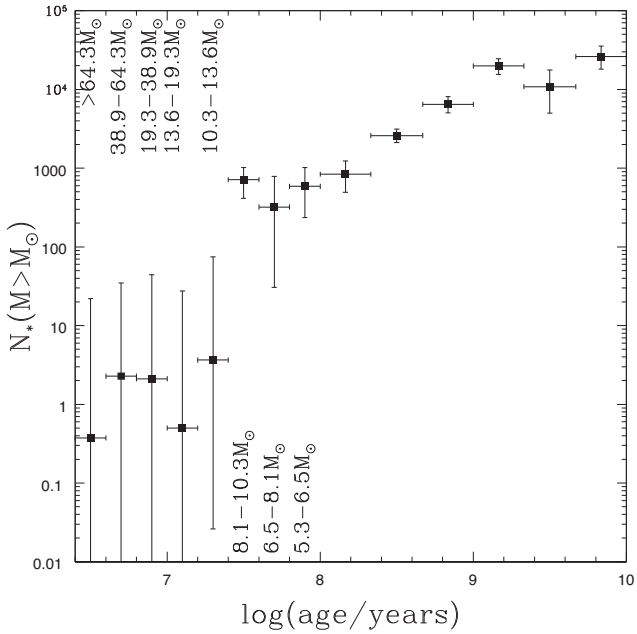

Figure 3. Inferred numbers N_i of $M > M_{\rm min} = {\rm M}_\odot$ stars formed for each age bin. This corresponds to the number of modelled stars shown in Fig. 2 divided by the fraction F_i of $M > M_{\rm min}$ stars which have $M_G > 0$ mag. The points show the median number of $M > M_{\rm min}$ stars associated with each age bin and the 90-per cent confidence range. The horizontal error bars span the bin widths and the mass range corresponding to the more massive age bins is listed. All uncertainties are highly correlated.

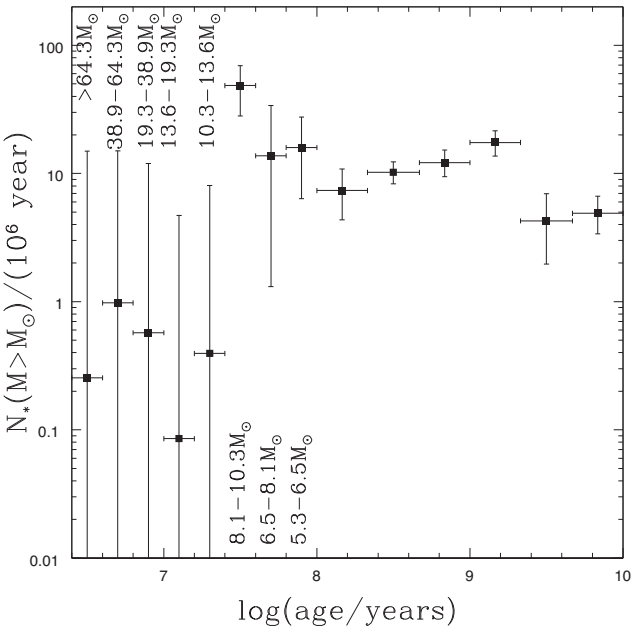

Figure 4. Rate of forming $M > M_{\rm min} = {\rm M}_\odot$ stars per million years for each age bin. This corresponds to the number of $M > M_{\rm min}$ stars N_i shown in Fig. 3 divided by the temporal bin width Δt_i. The points show the median star formation rate associated with each age bin and the 90-per cent confidence range. The horizontal error bars span the bin widths and the mass range corresponding to the more massive age bins is listed. All uncertainties are highly correlated.

stellar mass density of $(0.056 \pm 0.019)\,{\rm M}_\odot\,{\rm pc}^{-3}$ is remarkably close to the local estimate of $0.04\,{\rm M}_\odot\,{\rm pc}^{-3}$ (Flynn et al. 2006) given the huge correction required to go from the number of $M_G > 0$ mag stars to the total mass of stars – for the oldest bin, the ∼50 modelled $M_G > 0$ mag stars represent some $\sim 20\,000\,M > M_{\rm min} = {\rm M}_\odot$ stars which then correspond to some ∼200 000 stars in total.

Finally, Fig. 4 shows the star formation rates for each temporal bin as the number of $M > M_{\rm min} = {\rm M}_\odot$ stars formed per 10^6 yr. As discussed above, a formation rate of 10 $M > M_{\rm min} = {\rm M}_\odot$ stars per million years corresponds to a global Galactic star formation rate of order $0.04\,{\rm M}_\odot\,{\rm yr}^{-1}$, so the peak star formation rate of $\sim 0.3\,{\rm M}_\odot\,{\rm yr}^{-1}$ on a global basis is not impressive. The peak is, however, again found in the $10^{7.4}$–$10^{7.6}$ yr bin. The star formation rates in the younger bins are at least an order of magnitude lower, with even fewer new stars because the associated times Δt_i become shorter (i.e. the drop off in Fig. 3 is sharper than in Fig. 4).

Fig. 5 shows the model for the integral distribution of the selected stars in mass

$$D^j = \sum_i N_i D_i^j, \tag{8}$$

where the D_i^j are the mass distributions associated with each temporal bin. As expected from the distributions in Figs 1, the region contains few higher mass stars. We also show the integral distribution of the mass estimates from the SED models in Fig. 5. Broadly speaking they are in good agreement, although the results from the CMD models track the lower mass limits much more closely than the upper mass limits. As noted earlier, at roughly constant luminosity and temperature, there is a strong correlation between age and mass for these main-sequence B stars in the sense that the minimum mass estimates correspond to the maximum ages and *vice versa*. The CMD models strongly disfavour having significant numbers

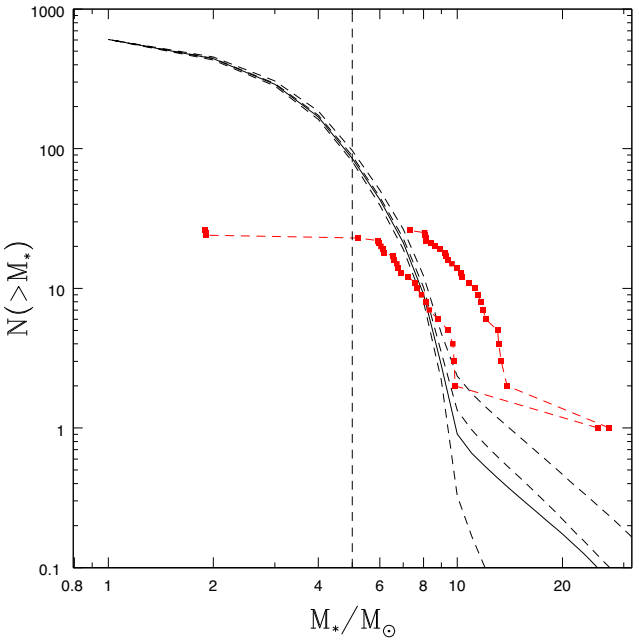

Figure 5. Mass distribution of the $M_G > 0$ mag stars. The black solid shows the maximum likelihood model and the dashed curves show the mean and 90 per cent confidence range for the integral distributions from the MCMC chains. This distribution should be nearly complete for masses above 5 $M_\odot$ (the vertical dashed line) and increasingly incomplete for lower masses. The red curves with points show the integral distributions for the minimum and maximum masses of the luminous stars with SED models from Table 2. The maximum mass star is γ^2 Vel. The maximum (minimum) masses correspond to younger (older) ages; and the CMD models strongly favour an older population and so match the minimum mass curve well.

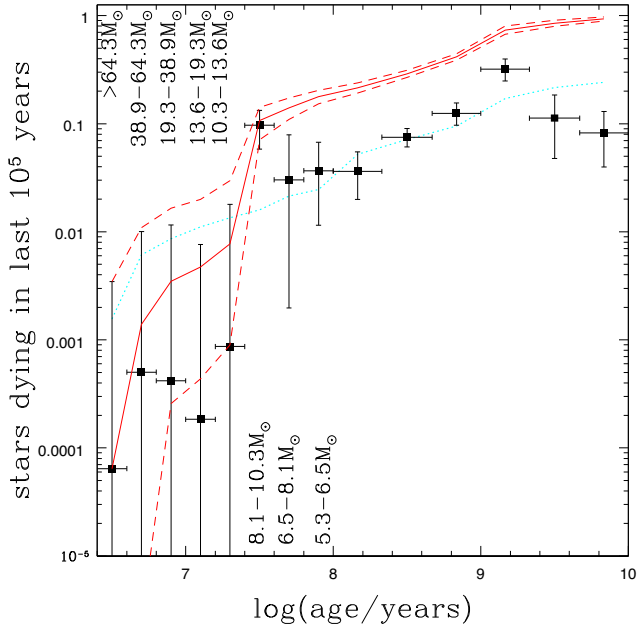

Figure 6. The number of stars dying in the last 10^5 yr for each age bin. The points show the probability for each bin and its 90-per cent confidence range. The horizontal error bars span the bin widths; and the mass range corresponding to each age bin is listed. The solid red curves shows the median integral distribution and the dashed curves show its 90-per cent confidence range. The arbitrarily normalized dotted cyan curve shows what the age distribution would be for a constant star formation rate. All uncertainties are highly correlated.

of stars with the young ages associated with the maximum mass estimates and strongly favour ages corresponding to the minimum mass estimates and so track the minimum mass estimates. The CMD models constrain the age distribution better than the SED models of individual stars.

The outlier in Fig. 5 is γ^2 Vel. The model mass distribution based on the CMD predicts only $\simeq 0.3$ ($\simeq 0.1$) stars with $M > 20\,M_\odot$ ($> 30\,M_\odot$). The existence of γ^2 Vel is not a huge statistical anomaly, as the likelihood of having one or more such stars is 26 per cent (10 per cent). However, in the CMD (Fig. 1), there are simply no other stars between where the $10^{7.5}$ yr isochrone (maximum mass 9.1 $M_\odot$) starts to turn-off the main sequence and γ^2 Vel. The absence of these stars drives the model to make γ^2 Vel moderately unlikely.

Fig. 6 shows the number of stars $N_i S_i \delta t$ (equation 3) predicted to have died in the last $\delta t = 10^5$ yr for each age bin. That the integral probability sums to near unity is happenstance – the distribution is not normalized. The probability for the ages leading to supernovae is dominated by the age range corresponding to initial masses of 8.1–10.3 $M_\odot$. Note that for the range of ages producing supernovae, the expected number of deaths in the last 10^5 yr is only $\sim$0.1 and so the time-scale for this volume to produce a supernovae is $\delta t \simeq 10^6$ yr, far longer than the lifetime of an SNR. This is not a statistical problem – we chose this volume because it contained an SNR. To estimate δt, we would have to analyse a much larger volume chosen without using any prior knowledge of the number of enclosed remnants.

Fig. 6 also shows what the prediction would be if the star formation rate was constant across all age bins, roughly normalized to the intermediate age bins where the estimated star formation rates are nearly constant (Fig. 4). The four youngest and two oldest bins have lower estimated SFRs, and so fewer stars are predicted to have died in the last 10^5 yr, while the $10^{7.4}$–$10^{7.6}$ yr bin has a higher SFR and more predicted deaths. The difference between the two curves represents the information added by using the local stellar population to infer the star formation history.

The probability of a star dying in the last $\delta t = 10^5$ yr is dominated by the older bins and the volume is likely to contain a number of young white dwarfs. Out of curiosity, we did a cursory search for candidates. Based on the MIST (Dotter 2016, Choi et al. 2016) evolutionary tracks, a $<10^5$ yr old white dwarf should be a very hot star with a luminosity $\sim 10^2\,L_\odot$. The Gaia EDR3 source ID#5319832121597913984 is the bluest and most luminous source near the tip of the usual white dwarf cooling sequence. It is flagged as a very high probability white dwarf candidate by Gentile Fusillo et al. (2019) but with no estimates of its physical properties. There are no UV or spectroscopic observations of it, but for an assumed temperature of 40 000 K, it would have a luminosity of $\sim 2\,L_\odot$. Since the luminosity scales linearly with the temperature on the Rayleigh–Jeans tail of the SED, this star has to be significantly older than 10^5 yr even at twice the temperature. There are five similarly blue but $\Delta M_G \sim -3$ mag more luminous stars (#5592257426113535104, #5411002594979483392, #5442024044243183232, #5512856125193586176, and #5539780553619327360) whose luminosities could be in the right range. Three of them are spectroscopically classified as hot sub-dwarfs (#5592257426113535104, Garrison & Hiltner 1973; #5442024044243183232, Barlow et al. 2013; #5539780553619327360, Kilkenny, Heber & Drilling 1988; one (#5411002594979483392) is spectroscopically classified as an A0

star, Nesterov et al. 1995, but this is difficult to reconcile with its location in the CMD), and #5512856125193586176 has no spectroscopic classifications. Possibly one of these latter two sources is a very young white dwarf masquerading as a hot subdwarf.

3.3 The progenitor of the Vela pulsar

To produce a final constraint on the mass of Vela's progenitor, we must consider three remaining issues. First, we have to put a minimum mass in by hand. When analysing a single region around one target, we cannot determine a minimum mass for explosion. This requires analysing many such regions both with and without SNRs. We must impose a minimum mass by simply dropping the older age bins. The obvious choice is to keep only the $10^{7.4}$–$10^{7.6}$ yr, with its maximum masses at death of 8.1–10.3 $M_\odot$, and younger bins. For single star evolution, this is the correct mass range for the cutoff. With binary evolution the next older bin can contribute through mergers of longer lived, lower mass stars (see e.g. Zapartas et al. 2017). Retaining this next older bin would only strengthen our final conclusion that the progenitor was significantly less massive than 20 $M_\odot$. The change would be modest because many fewer stellar deaths are expected from this age bin than from the $10^{7.4}$–$10^{7.6}$ yr bin (see Fig. 6).

In our formalism, the number of stellar deaths is $N_i S_i \delta t$, where S_i is independent of δt. For our final result, we want the relative probabilities of the age bins with no dependence on δt. The probability that the progenitor came from bin i and no other bin j is

$$\begin{aligned} P(i\&!j) &= N_i S_i \delta t \exp(-N_i S_i \delta t) \Pi_{i\neq j} \exp(-N_j S_j \delta t) \\ &= N_i S_i \delta t \, \Pi_{\rm all} \exp(-N_J s_j \delta_j) \end{aligned} \tag{9}$$

('$i\&!j$' is a shorthand for 'INCLUDE i AND NOT j'). The total probability summed over all the bins is

$$P_{tot} = \sum_i P(i\&!j) = \delta t \left[\sum_{\rm all} N_i S_i\right] \exp\left(-\delta t \sum_{\rm all} N_i S_i\right) \tag{10}$$

and thus the normalized probability for each bin of

$$P_{tot}^{-1} P(i\&!j) = N_i S_i \left[\sum_{\rm all} N_i S_i\right]^{-1}, \tag{11}$$

is independent of δt as desired. Basically, this just corresponds to normalizing the integral probability distribution so that the total probability is unity.

Finally, we have a maximum likelihood solution and all the MCMC samples, each of which represents a realization of the integral probability distribution. We could go to each age bin, sort these distributions, and report a median and some range, say 90-per cent confidence, but it is unclear how to interpret this. What does it mean to say there is a 5-per cent chance that there is a 10-per cent chance that the progenitor was younger than the age of some bin? There really should be only one distribution which incorporates this information. We are really combining the $N_{\rm MCMC}$ results of the MCMC chains, each of which has a probability of $N_{\rm MCMC}^{-1}$, and each trial predicts a probability for the age of the progenitor. The way to combine them is to sum the probability the trial predicts for the age bin weighted by the probability of the trial – in short, the final probability distribution is simply the average of the MCMC samples.

Fig. 7 shows these final probability distributions as a function of the radius R of the sphere used to select the stars. Recall that the results so far have all been for $R < 125$ pc. The maximum likelihood age distributions modestly favour older, lower mass

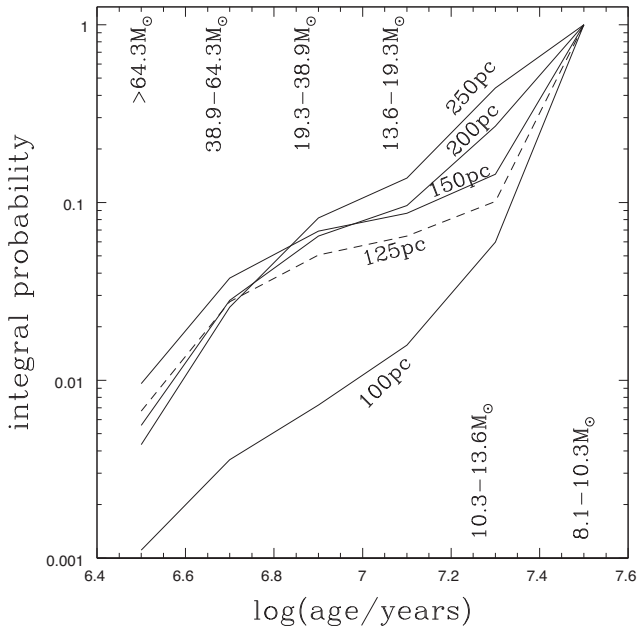

Figure 7. Integral probability distributions for the age of the progenitor of Vela as a function of the radius R used to select the stars. The dashed curve is for the $R = 125$ pc radius used until now. The large difference between this distribution and the distribution for $R = 100$ pc is due to the inclusion of γ^2 Vel in the larger sphere.

progenitors compared to these distributions. For $R < 100$ pc, a low mass progenitor is very strongly favoured with a 94-per cent probability of it coming from the lowest mass bin (8.1–10.3 $M_\odot$). However, as we discussed in Section 2, this sphere probably only contains ∼2/3 of the stars born within a similar radius. If we increase the radius to $R < 125$ pc, the structure of the distribution changes considerably, and this is entirely driven by the inclusion of γ^2 Vel. The probability of the oldest age bin is still high (90 per cent), but the probability of an age bin corresponding to a progenitor more massive than $> 20\,M_\odot$ increases by almost an order of magnitude. None the less, the probability of a progenitor less massive than 20 $M_\odot$ is still 95 per cent. Expanding the sphere still further primarily increases the probability of the 13.6–19.3 and 10.3–13.6 $M_\odot$ progenitor bins relative to the 8.1–10.3 $M_\odot$ bin. The probability of being less massive than 20 $M_\odot$ is still 90 per cent.

In fact, γ^2 Vel is associated with a concentrated cluster of pre-main-sequence stars with a very low velocity dispersion (e.g. Franciosini et al. 2018). This means that associating the progenitor of Vela with the formation of γ^2 Vel and its cluster requires the progenitor to have been a runaway star. To explore this, we used the fiducial runaway model from Renzo et al. (2019) and estimated the distance the surviving stars from disrupted binaries could travel in the time left for their current evolutionary phase. Since we now have an isolated star, this will be close to the remaining lifetime of the star. Because of mass transfer, we examined the fraction of stars which could travel more than 100 pc (the distance from γ^2 Vel to the pulsar) in bins of either the zero age main sequence (ZAMS) mass or the mass after the binary is disrupted.

For the ZAMS mass and no restriction on the mass of the star which died to disrupt the binary, the chances of traveling 100 pc were significant only for 10–15 $M_\odot$ (20 per cent) and 15–20 $M_\odot$ (5 per cent) stars. Stars with higher post-disruption masses could do so because they are initially lower mass stars that were mass

gainers when the primary began to evolve. Even so, only 7.6, 2.7, and 2.2 per cent of stars with post-disruption masses of 20–25, 25–30, and 30–35 $M_\odot$ could travel 100 pc. Demanding a high ($M > 30\,M_\odot$) ZAMS mass primary helps only modestly. Thus, a volume including γ^2 Vel does significantly increase the probability of a higher mass ($\gtrsim 20\,M_\odot$) progenitor, but a Vela progenitor formed in the cluster associated with γ^2 Vel would (a) have to be a runaway star from a disrupted binary, and (b) would have to have a statistically unlikely runaway velocity.

4 DISCUSSION

The environment of the Vela pulsar is dominated by B stars with only one nearby O star, γ^2 Vel. If we consider only stars within $R < 100$ pc of Vela, the most likely (95 per cent) age range for its progenitor is $10^{7.4}$–$10^{7.6}$ yr corresponding to a mass range of 8.1–10.3 $M_\odot$. There is clearly a local burst of star formation associated with this age bin. For these ages and the observed velocity dispersions of the stars, a radius of $R < 100$ pc will not encompass all of the stars formed within 50–100 pc of the progenitor. Any larger sphere encompasses the most massive nearby star, the O star plus WR star binary γ^2 Vel. So for $R < 125$ pc, there is still a 90-per cent probability of associating the progenitor with the $10^{7.4}$–$10^{7.6}$ yr age bin, but there is now a 5-per cent chance of an age allowing masses $> 20\,M_\odot$. However, γ^2 Vel is associated with a very low velocity dispersion cluster, so for the progenitor to be that massive, it would also need to be a runaway star from a disrupted binary with an unusually high velocity based on the models of Renzo et al. (2019).

We have assumed single star evolution models in this analysis. We know that Vela itself was not a binary or triple at the time of its death (Fraser & Boubert 2019; Kochanek 2021) down to companion mass limits $\lesssim M_\odot$. This does not rule out the progenitor as a merger remnant or as an unbound secondary from a previous explosion. As a merger remnant or an unbound secondary that gained significant mass through mass transfer, we have underestimated the probability of a low-mass progenitor because we imposed the minimum-mass/maximum-age limit by hand since it cannot be determined by analysing a single system. The changes from including the next lower mass bin would not be huge, because the star formation rate estimated for this next bin is much lower than for the $10^{7.4}$–$10^{7.6}$ yr age bin.

The effect of binaries on inferred masses is generally modest except for near twin binaries. While it is beyond the scope of this present study, it might be possible to quantitatively explore the numbers and properties of the massive star binary population associated with Vela. Certainly, many of the nearby massive stars are known binaries (see Table 2). What is unclear and difficult to determine is the degree to which the samples are complete or well-characterized. To the extent that neglecting binaries only leads to mass overestimates and that our conclusion is that the progenitor of Vela was low mass, a full accounting for binaries would only strengthen our conclusion. But the effect would be modest – probably 10 per cent at most.

As noted in the introduction, the two fundamental limitations to applying this method in the Galaxy are estimating the distance to the SNR and extinction. There are three additional systems which can be analysed easily. G180.0−01.7 is associated with the radio pulsar PSR J0538+2817, which has a VLBI parallax (Ng et al. 2007; Chatterjee et al. 2009). In Kochanek (2021), we examined the properties of the nearby luminous stars but did not carry out a formal analysis as done here for Vela. G205.5+0.00.5 (Monoceros Loop) and G284.3−01.8 both contain neutron star high-mass X-ray binaries (Hinton et al. 2009; Corbet et al. 2011) and the stellar companions have *Gaia* parallaxes (see Kochanek 2021). Unfortunately, the interacting (probably) black hole binary SS 433 (see the review by Margon 1984) in G039.7−02.0 is likely too distant ($\varpi^{-1} = 8.5$ kpc) to use *Gaia* parallaxes to trivially select stars in a ∼100-pc sphere around the binary. The Gaia EDR3 parallax of SS 433 is also in strong ($\sim 5\sigma$) disagreement with the distances estimated from kinematic models of the relativistic jets (Blundell & Bowler 2004; Marshall et al. 2013). As discussed in Kochanek (2021), the success of Cha, Sembach & Danks (1999) in determining the distance to the Vela remnant based on the distance at which stars began to show absorption features from the SNR provides a simple observational approach to better determining the distances to other remnants.

If we consider the 165 pulsars with parallaxes in the ATNF Pulsar Catalogue (Manchester et al. 2005), the vast majority cannot be analysed using this method because the formation region cannot be well-localized. In particular, the only available age estimate is the spin down age which at best estimates the time of explosion to within a factor of 2. If we require that the projected distance travelled in the spin-down age is less than 100 pc, only 10 pulsars are left after excluding Vela. Because the proper motions represent two components of the kick velocity while the motion along the line of sight contains only one component, the line-of-sight motions should be less of a problem. If we assume a typical neutron star kick velocity of 265 km s^{-1} (Hobbs et al. 2005), the typical line-of-sight distance travelled in the spin-down time for the pulsars with transverse motions less than 100 pc ranges from 24 to 152 pc. If we require this line-of-sight motion to be <100 pc and restrict the parallax distance to be <2 kpc, we are left with four systems other than Vela (J0157+6212, J0633+1746, J0659+1414, and J2032+4127). This would be a sample biased towards supernovae with low kick velocities.

In the absence of good parallaxes, the alternative is to simply look at all the stars projected within a fixed projected separation from the SNR over some broad line of sight distance range consistent with estimates for the distance to the SNR. This is what is done for all the extragalactic analyses since there is no possibility of using parallaxes to remove the foreground and background contamination. However, while some of the external galaxies that have been examined are highly inclined (e.g. Andromeda at ∼13°), none have as unfavourable geometry for minimizing contamination as we face for examining Galactic SNRs. Which Galactic SNRs are suitable for such an analysis will depend on their Galactic coordinates.

Related to this is the question of completeness and contamination in analyses of stellar populations near extragalactic supernovae and remnants. We can use our nearly complete knowledge of the environment around Vela to evaluate the 50-pc projected search region used by Jennings et al. (2012) and subsequent papers. We again restrict ourselves to the more massive stars using the magnitude and colour cuts described in Section 2. We can continue to use our original selection in a 250-pc sphere because massive stars have a small scale height. We transform the stellar positions to axes aligned with Galactic coordinates, select stars in a sphere around Vela, and then count stars using their positions 10^7 yr ago in circles centered on their median position as if we were looking down on the plane of the Galaxy (i.e. we ignore the distance of the star from the Galactic plane). As before, there are 19 stars in a 50-pc sphere around Vela, while a 50-pc circle centered on their median position 10^7 yr ago contains only nine of them along with 22 other stars, so the completeness is 47 per cent and the contamination is 79 per cent. Table 1 summarizes the results for several other radii and for an age of $10^{7.5}$ yr.

If the environment of Vela is typical, a 50-pc projected search radius includes almost none of the $\gtrsim 5\,M_\odot$ stars that were within 50 pc of the progenitor at birth – the stars within this radius are overwhelmingly stars which were more distant from the progenitor at birth. A larger, 100-pc projected search radius does capture a reasonable fraction of the stars born within 100 pc of the progenitor, but they are still only about half of the stars within that projected radius. This strongly suggests that this method of analysis cannot estimate the progenitor properties for individual SNRs or supernovae in external galaxies – it can only statistically estimate the progenitor properties for large ensembles of targets. Even with complete 3D information, as we have for Vela, there are significant problems with completeness and contamination in such small regions on the 30 million yr time-scale before $\simeq 10\,M_\odot$ stars explode.

ACKNOWLEDGEMENTS

The author thanks K. Auchettl, J. Johnson, M. Pinsonneault, K. Stanek, and T. Thompson for discussions. CSK is supported by NSF grants AST-1908570 and AST-1814440. This research has made use of the VizieR catalogue access tool, CDS, Strasbourg, France (DOI : 10.26093/cds/vizier). The original description of the VizieR service was published in Ochsenbein, Bauer & Marcout (2000). This research has made use of the SIMBAD (Wenger et al. 2000) data base, operated at CDS, Strasbourg, France.

DATA AVAILABILITY STATEMENT

All data used in this paper are publicly available.

REFERENCES

Adams S. M., Kochanek C. S., Gerke J. R., Stanek K. Z., Dai X., 2017a, MNRAS, 468, 4968
Adams S. M., Kochanek C. S., Gerke J. R.,Stanek K. Z., 2017b, MNRAS, 469, 1445
Aschenbach B., Egger R., Trümper J., 1995, Nature, 373, 587
Auchettl K., Lopez L. A., Badenes C., Ramirez-Ruiz E., Beacom J. F., Holland-Ashford T., 2019, ApJ, 871, 64
Badenes C., Harris J., Zaritsky D., Prieto J. L., 2009, ApJ, 700, 727
Barlow B. N. et al., 2013, MNRAS, 430, 22
Basinger C. M., Kochanek C. S., Adams S. M., Dai X.,Stanek K. Z., 2020, MNRAS, 508, 1156
Beasor E. R., Davies B., Smith N., van Loon J. Th., Gehrz R. D., Figer D. F., 2020, MNRAS, 492, 5994
Belczynski K. et al., 2020, A&A, 636, 104
Blundell K. M., Bowler M. G., 2004, ApJ, 616, L159
Bollig R., Yadav N., Kresse D., Janka H.-T.,Müller B., Heger A., 2021, ApJ, 915, 28
Bovy J., Rix H.-W., Green G. M., Schlafly E. F., Finkbeiner D. P., 2016, ApJ, 818, 130
Breivik K. et al., 2020, ApJ, 898, 71
Bressan A., Marigo P., Girardi L., Salasnich B., Dal Cero C., Rubele S., Nanni A.,2012, MNRAS, 427, 127
Burrows A., Radice D., Vartanyan D., Nagakura H., Skinner M. A., Dolence J. C., 2020, MNRAS, 491, 2715
Castelli F., Kurucz R. L., 2003, Modelling Stellar Atmos., 210, 20P
Chatterjee S. et al., 2009, ApJ, 698, 250
Chawla C., Chatterjee S., Breivik K. et al., 2021, preprint (arXiv:2110.05979)
Cha A. N., Sembach K. R., Danks A. C., 1999, ApJ, 515, L25
Choi J., Dotter A., Conroy C., Cantiello M., Paxton B., Johnson B. D., 2016, ApJ, 823, 102
Corbet R. H. D. et al., 2011, Astron. Telegram, 3221
Cousins A. W. J., 1971, R. Obs. Ann., 7
Cutri R. M., Skrutskie M. F., van Dyk S. et al., 2003, The IRSA 2MASS All-Sky Point Source Catalog, NASA/IPAC Infrared Science Archive. Oxford Univ. Press
Davies B., Beasor E. R., 2020, MNRAS, 493, 468
Díaz-Rodríguez M., Murphy J. W., Rubin D. A., Dolphin A. E., Williams B. F., Dalcanton J. J., 2018, ApJ, 861, 92
Díaz-Rodríguez M., Murphy J. W., Williams B. F., Dalcanton J. J., Dolphin A. E., 2021, MNRAS, 506, 781
Dodson R., Legge D., Reynolds J. E., McCulloch P. M.,2003, ApJ, 596, 1137
Dotter A., 2016, ApJS, 222, 8
Drimmel R., Cabrera-Lavers A., López-Corredoira M., 2003, A&A, 409, 205
Ducati J. R., 2002, VizieR Online Data Catalog
Eldridge J. J., Langer N., Tout C. A., 2011, MNRAS, 414, 3501
Eldridge J. J., Fraser M., Smartt S. J.,Maund J. R.,Crockett R. M., 2013, MNRAS, 436, 774
Eldridge J. J., Stanway E. R., Xiao L., McClelland L. A. S., Taylor G., Ng M., Greis S. M. L., 2017, PASA, 34, e058
Elitzur M., Ivezić Ž., 2001, MNRAS, 327, 403
Ertl T. et al., 2016, ApJ, 818, 124
Farrell E. J. et al., 2020, MNRAS, 494, L53
Fernández R. et al., 2018, MNRAS, 476, 2366
Flynn C. et al., 2006, MNRAS, 372, 1149
Folatelli G. et al., 2016, ApJ, 825, L22
Franciosini E. et al., 2018, A&A, 616, L12
Fraser M., Boubert D., 2019, ApJ, 871, 92
Fryer C. L. et al., 2012, ApJ, 749, 91
Gaia Collaboration et al., 2016, A&A, 595, A1
Gaia Collaboration et al., 2021, A&A, 649, A1
Garrison R. F., Hiltner W. A., 1973, ApJ, 179, L117
Gentile Fusillo N. P. et al., 2019, MNRAS, 482, 4570
Gerke J. R., Kochanek C. S., Stanek K. Z., 2015, MNRAS, 450, 3289
Ghosh S., Wolfe N., Fröhlich C., 2021, preprint (arXiv:2107.13016)
Gilmozzi R. et al., 1987, Nature, 328, 318
Green G. M. et al., 2019, ApJ, 887, 93
Groh J. H. et al., 2013, A&A, 558, A131
Gustafsson B. et al., 2008, A&A, 486, 951
Hinton J. A. et al., 2009, ApJ, 690, L101
Hobbs G., Lorimer D. R., Lyne A. G., Kramer M., 2005, MNRAS, 360, 974
Hoffleit D., Warren W. H., 1995, VizieR Online Data Catalog, V/50x
Jacovich T. et al., 2021, ApJ, 914, 41
Jennings Z. G. et al., 2012, ApJ, 761, 26
Jennings Z. G. et al., 2014, ApJ, 795, 170
Johnson S. A., Kochanek C. S., Adams S. M., 2017, MNRAS, 472, 3115
Johnson H. L. et al., 1966, Commun. Lunar Planet. Lab., 4, 99
Kilkenny D., Heber U., Drilling J. S., 1988, South African Astron. Obs. Circ., 12, 1
Kilpatrick C. D. et al., 2021, MNRAS, 504, 2073
Kochanek C. S., 2014, ApJ, 785, 28
Kochanek C. S., 2020, MNRAS, 493, 4945
Kochanek C. S., 2021, MNRAS, 507, 5832
Kochanek C. S. et al., 2008, ApJ, 684, 1336
Kochanek C. S., Khan R., Dai X., 2012, ApJ, 759, 20
Koplitz B. et al., 2021, ApJ, 916, 58
Kroupa P., 2001, MNRAS, 322, 231
Lada C. J., Lada E. A., 2003, ARA&A, 41, 57
Large M. I., Vaughan A. E., Mills B. Y., 1968, Nature, 220, 340
Lovegrove E., Woosley S. E., 2013, ApJ, 769, 109
Lyne A. G. et al., 1996, Nature, 381, 497
Manchester R. N. et al., 2005, AJ, 129, 1993
Margon B., 1984, ARA&A, 22, 507
Marigo P. et al., 2013, MNRAS, 434, 488
Marshall D. J. et al., 2006, A&A, 453, 635
Marshall H. L. et al., 2013, ApJ, 775, 75
Mermillod J. C., 1977, Geneva: Observatory, 1977
Morel M., Magnenat P., 1978, A&ASup, 34, 477
Nadezhin D. K., 1980, Ap&SS, 69, 115
Neckel T., Klare G., 1980, A&ASup, 42, 251

Nesterov V. V. et al., 1995, A&AS
Neustadt J. M. M., Kochanek C. S., Stanek K. Z., Basinger C., Jayasinghe T., Garling C. T., Adams S. M., Gerke J., 2021, MNRAS, 508, 516
Ng C.-Y., Romani R. W., Brisken W. F., Chatterjee S., Kramer M., 2007, ApJ, 654, 487
North J. R., Tuthill P. G., Tango W. J., Davis J., 2007, MNRAS, 377, 415
O'Connor E., Ott C. D., 2011, ApJ, 730, 70
Ochsenbein F., Bauer P., Marcout J., 2000, A&AS, 143, 23
Pan K.-C., Liebendörfer M., Couch S. M., Thielemann F.-K., 2021, ApJ, 914, 140
Pastorelli G. et al., 2020, MNRAS, 498, 3283
Pejcha O., Thompson T. A., 2015, ApJ, 801, 90
Perryman M. A. C. et al., 1997, A&A, 500, 501
Renzo M. et al., 2019, A&A, 624, A66
Riley J. et al., 2021, MNRAS, 505, 663
Salpeter E. E., 1955, ApJ, 121, 161
Sarbadhicary S. K., Badenes C., Chomiuk L., Caprioli D., Huizenga D., 2017, MNRAS, 464, 2326
Smartt S. J., 2009b, ARA&A, 47, 63
Smartt S. J., 2015, PASA, 32, e016
Smartt S. J., Eldridge J. J., Crockett R. M., Maund J. R., 2009a, MNRAS, 395, 1409
Sukhbold T., Adams S., 2020, MNRAS, 492, 2578
Sukhbold T., Ertl T., Woosley S. E., Brown J. M., Janka H.-T., 2016, ApJ, 821, 38
Sukhbold T., Woosley S. E., Heger A., 2018, ApJ, 860, 93
Thompson G. I., Nandy K., Jamar C. et al., 1978, 'Catalogue of stellar ultraviolet fluxes: a compilation of absolute stellar fluxes measured by the Sky Survey Telescope (S2/68) aboard the ESRO satellite TD-1'
Tokovinin A., 2018, ApJS, 235, 6
Tonry J. L. et al., 2018, ApJ, 867, 105
van Leeuwen F., 2007, A&A, 474, 653
Verbiest J. P. W., Weisberg J. M., Chael A. A. et al., 2012, ApJ, 755, 39
Walmswell J. J., Eldridge J. J., 2012, MNRAS, 419, 2054
Wenger M. et al., 2000, A&AS, 143, 9
Wesselius P. R., van Duinen R. J., de Jonge A. R. W., Aalders J. W. G., Luinge W., Wildeman K. J., 1982, A&AS, 49, 427
Williams B. F., Hillis T. J., Murphy J. W., Gilbert K.,Dalcanton J. J., Dolphin A. E.,2018, ApJ, 860, 39
Williams B. F. et al., 2019, ApJ, 881, 54
Zacharias N., Monet D. G., Levine S. E. et al., 2005, VizieR Online Data Catalog, I/297
Zapartas E. et al., 2017, A&A, 601, A29

This paper has been typeset from a TEX/LATEX file prepared by the author.